

OGLE14-073 – a promising pair-instability supernova candidate

Alexandra Kozyreva,^{1★} Markus Kromer,^{2,3★} Ulrich M. Noebauer⁴ and Raphael Hirschi^{5,6}

¹*The Sackler School of Physics and Astronomy, Tel Aviv University, 69938 Tel Aviv, Israel*

²*Zentrum für Astronomie der Universität Heidelberg, Institut für Theoretische Astrophysik, D-69120 Heidelberg, Germany*

³*Heidelberger Institut für Theoretische Studien, D-69118 Heidelberg, Germany*

⁴*Max-Planck-Institut für Astrophysik, Karl-Schwarzschild-Straße 1, D-85748 Garching, Germany*

⁵*Astrophysics group, Keele University, Keele, Staffordshire ST5 5BG, UK*

⁶*Kavli IPMU (WPI), University of Tokyo, Kashiwa, Chiba 277-8583, Japan*

Accepted 2018 April 13. Received 2018 March 29; in original form 2018 February 17

ABSTRACT

The recently discovered bright Type II supernova OGLE14-073 evolved very slowly. The light curve rose to maximum for 90 d from discovery and then declined at a rate compatible with the radioactive decay of ^{56}Co . In this study, we show that a pair-instability supernova is a plausible mechanism for this event. We calculate explosion models and light curves with the radiation hydrodynamics code STELLA starting from two $M_{\text{ZAMS}} = 150 M_{\odot}$, $Z = 0.001$ progenitors. We obtain satisfactory fits to OGLE14-073 broad-band light curves by including additional ^{56}Ni in the centre of the models and mixing hydrogen down into the inner layers of the ejecta to a radial mass coordinate of $10 M_{\odot}$. The extra ^{56}Ni required points to a slightly more massive progenitor star. The mixing of hydrogen could be due to large-scale mixing during the explosion. We also present synthetic spectra for our models simulated with the Monte Carlo radiative transfer code ARTIS. The synthetic spectra reproduce the main features of the observed spectra of OGLE14-073. We conclude that OGLE14-073 is one of the most promising candidates for a pair-instability explosion.

Key words: radiative transfer – stars: massive – supernovae: general; supernovae: individual: OGLE14-073.

1 INTRODUCTION

OGLE14-073 is a unique supernova (SN) event which was discovered long before its peak (Blagorodnova et al. 2014; Wyrzykowski et al. 2014; Terreran et al. 2017). It was classified as a bright hydrogen-rich Type II SN at redshift $z = 0.1225$. Thanks to an extensive follow-up campaign, it has good data coverage, starting from 90 d before peak magnitude in the *I* band. Recently, Moriya, Terreran & Blinnikov (2018) and Dessart & Audit (2017) suggested fallback accretion or a magnetar as the powering engine of this bright SN.

However, the long rise to peak could also indicate a high ejecta mass (Terreran et al. 2017 estimate $M_{\text{ej}} \sim 60 M_{\odot}$). This can only be realized if the initial mass of the progenitor star was above at least $100 M_{\odot}$. From a theoretical point of view, it is well known that stars with initial mass range between 140 and $260 M_{\odot}$ undergo pair instability and explode as pair-instability supernovae (hereafter

PISN; Barkat, Rakavy & Sack 1967; Rakavy & Shaviv 1967). Depending on the amount of radioactive ^{56}Ni produced, the SN may be either sub- or superluminous (Gilmer et al. 2017).

The long rise of OGLE14-073 and the presence of H Balmer lines throughout observations covering more than 150 d require a massive H-rich ejecta. The peak luminosity in combination with an assumption about the time of explosion constrains the amount of ^{56}Ni which powers the light curve (Arnett 1982). Unfortunately, the explosion time is quite uncertain for OGLE14-073. According to the findings by Kozyreva et al. (2016), the peak luminosity of $9.6 \pm 0.2 \times 10^{42} \text{ erg s}^{-1}$ for OGLE14-073 (Terreran et al. 2017) requires $1.3 M_{\odot}$ of ^{56}Ni . Terreran et al. (2017) derive a lower limit for the ^{56}Ni mass of $0.47 M_{\odot} \pm 0.02 M_{\odot}$ assuming that the explosion occurred just before the first detection.

In a pair-instability explosion, there is a strong correlation between the mass of the final carbon–oxygen-rich core (CO core) and the ^{56}Ni yield (see e.g. Heger & Woosley 2002, and references therein), because nickel production depends on the degree of compression during the collapse phase. The larger the CO core mass, the deeper the gravitational potential reached during the pair-instability phase. In turn, higher density and temperature are reached at max-

* E-mail: sasha.kozyreva@gmail.com (AK); markus.kromer@h-its.org (MK)

imum compression, releasing more nuclear energy and producing higher yields of ^{56}Ni . Most of the helium-rich core is burnt into carbon and oxygen in PISN progenitors, leaving a narrow He-shell on top of the core, which only amounts to a few solar masses (see e. g. Yusof et al. 2013). Thus the final helium core mass roughly equals the CO core mass. In PISN models, stars with helium cores of 80–90 M_{\odot} generate 0.5–1.3 M_{\odot} of ^{56}Ni . Note that the nickel yield varies rapidly at the lower end of the PISN mass range. For example, a model with a 70 M_{\odot} He core (CO-core of 64 M_{\odot}) gives 0.02 M_{\odot} of ^{56}Ni , while a model with an He core of 90 M_{\odot} (CO-core of 82 M_{\odot}) produces already 1.3 M_{\odot} of ^{56}Ni . This implies that a 25 per cent increase in the helium core mass corresponds to almost two orders of magnitude difference in the ^{56}Ni yield (Heger & Woosley 2002). Hence, assuming that OGLE14-073 exploded as a PISN, its progenitor is expected to be a very massive star with a final helium core mass in the range of 80–90 M_{\odot} .

In the present study, we examine a possible PISN origin of OGLE14-073. In particular, we construct ejecta configurations based on two existing self-consistent PISN models to explain the light curves and spectra of OGLE14-073. Details of our explosion models and the techniques to model light curves and spectra are given in Section 2. In Section 3, we present synthetic observables for our best-fitting model and discuss how the light curve properties depend on different progenitor and explosion parameters before concluding the study in Section 4.

2 MODELLING OGLE14-073

2.1 Explosion models

Our models are based on two very massive non-rotating star models with $M_{\text{ZAMS}} = 150 M_{\odot}$ at a metallicity $Z = 0.001$, evolved from the zero age main sequence (ZAMS) until the start of the pair-instability phase with stellar evolution codes. The two models, 150M and P150, were evolved with `BEC` (Langer et al. 2007; Kozyreva, Yoon & Langer 2014b) and `GENEC` (Ekström et al. 2012; Yusof et al. 2013), respectively. Abundances in the original `GENEC` stellar evolution model P150 are scaled from solar metallicity ($Z = 0.014$) down to $Z = 0.001$ and alpha-enhanced in most cases, following observational constraints (Lodders 2003). Note that although both models have the same total metallicity, it is distributed differently on to the various elements. In particular, the calcium abundance is zero in 150M but 1.5×10^{-6} in P150.

Pair-instability explosions of the original models 150M and P150 were carried out with `BEC` and `FLASH` (Fryxell et al. 2000; Dubey et al. 2009; Chatzopoulos, Wheeler & Couch 2013; Chatzopoulos et al. 2015), respectively. The models 150M and P150 have helium core masses of 73 M_{\odot} and 83 M_{\odot} , respectively. Both models build up equally massive CO-cores of 64 M_{\odot} . In the explosion, only small amounts of ^{56}Ni are produced, namely 0.04 M_{\odot} in 150M and 0.003 M_{\odot} in P150. Consequently, the resulting light curves are dominated by cooling processes and do not show a peak powered by ^{56}Ni (Kozyreva et al. 2014a; Gilmer et al. 2017). Thus, these models are not compatible with OGLE14-073 since its peak luminosity seems to require about 1.3 M_{\odot} of ^{56}Ni .

However, rotation-induced mixing would effectively increase the CO-core mass. Therefore, rotating siblings of our 150 M_{\odot} models would end up with higher mass CO-cores and, in turn, yield more ^{56}Ni in a PISN explosion. For example, a $Z = 0.001$, 150 M_{\odot} rotating model computed with `GENEC` develops an 85 M_{\odot} helium core and an 80 M_{\odot} CO-core (R. Hirschi, private communication; Yusof et al. 2013). Besides that, more massive stars at slightly

lower metallicity ($Z < 0.001$) retain the hydrogen–helium envelope similar to 150M or P150 (R. Hirschi, N. Yusof, private communication). Therefore, we decided that using 150M and P150 as reference models is a reasonable starting point.

Ideally, a large grid of models would be computed, with initial masses between 150 and 200 M_{\odot} (^{56}Ni yield from 0.003 M_{\odot} up to 13 M_{\odot}), with varying initial metallicities and different degrees of rotation to find the best match to OGLE14-073. However, computing the evolution of very massive star models is very challenging due to the loose gravitational binding of the hydrogen-rich envelope and the proximity to the Eddington limit. Furthermore, mass loss is uncertain in these stars and they may experience large, η -Carinae-like, mass-loss episodes (Vink 2015). Given all these complications, we adopt a reverse-engineering approach in this study to find out which modifications of the original models would enable a fit to the observed properties of OGLE14-073. The modifications made to the original models are given in Table 1 and we add suffixes to the original model names to identify them. We explain below in more detail the various modifications made and the underlying motivations.

In the original observational paper by Terreran et al. (2017), the authors find a number of similarities between OGLE14-073 and SN 1987A. In particular, $\text{H}\alpha$ is observed during the whole observational period. Hence, the chemical structure of the OGLE14-073 ejecta might resemble that of SN 1987A. Studies of SN 1987A conclude that hydrogen was mixed deep into the ejecta and that ^{56}Ni was mixed into ejecta regions far away from the centre (Utrobin 1993). Such a mixing pattern has been confirmed in multi-dimensional simulations of core collapse SNe (e.g. Wongwathanarat, Müller & Janka 2015). Similar mixing processes might be active in PISN. Indeed, 2.5-D simulations of rotating PISNe by Chatzopoulos et al. (2013) show the formation of Rayleigh–Taylor instabilities and asymmetries that lead to mixing in the ejecta. Based on this and the similarities between OGLE14-073 and SN 1987A, we explored whether the presence of hydrogen in OGLE14-073 might be explained by artificially mixing hydrogen deep into the ejecta in both explosion models. We found that modified versions of models 150M and P150 with a hydrogen mass fraction of 0.1 down to a mass coordinate $M_r = 10 M_{\odot}$ produce bolometric light curves in good agreement with OGLE14-073.

The best-fitting models of SN 1987A have ^{56}Ni mixed throughout the entire ejecta (Nomoto et al. 1988). Thus, we also explored the effect of mixing ^{56}Ni outward in the model P150. We constructed models, in which ^{56}Ni was smeared out uniformly inside the inner 10, 30 and 50 solar masses, but found that this mixing does not improve the match between the resulting synthetic light curves and OGLE14-073 (see discussion in Section 3).

Finally, we lowered the hydrogen-to-helium mass fraction ratio in the outer shells of the model 150M ($\text{H}:\text{He} \simeq 1:4$ in the original model, while we set $\text{H}:\text{He} \simeq 1:8$), to reduce the high cooling emission after the shock breakout. For the same reason, i.e. to reduce the strong cooling signature, model 150M was truncated at a radius $R = 2000 M_{\odot}$ (the original radius of 150M is 3475 M_{\odot}). In Fig. 1, we show the radial distribution of hydrogen, ^{56}Ni and a few other selected chemical species for our best-fitting models 150M-bf and P150-bf, and compare them to the distribution of hydrogen and ^{56}Ni in the original models 150M and P150.

2.2 Light-curve modelling

We follow the SN explosion and model the light curve with the one-dimensional multigroup radiation hydrodynamics code `STELLA`

Table 1. Characteristics of the PISN models in the present study. Explosion energy is in foe, where 1 foe = 10^{51} erg. All masses and mass coordinates are in solar masses. For some of the models featuring hydrogen down-mixing and up-mixing of ^{56}Ni , the constant mass fractions of these elements are provided in parenthesis.

Model	Radius [R_{\odot}]	M_{tot} [M_{\odot}]	M_{H} [M_{\odot}]	H-mix down to M_r [M_{\odot}]	M_{Ni} [M_{sun}]	Ni-mix up to M_r [M_{\odot}]	E_{expl} [foe]	Notes
150M	3450	93	4.9	–	0.03	6	5	Original (Kozyreva et al. 2014)
150M-3000R	3000	90	3.9	30	1.18	6	9	
150M-14foe	2000	86	9.1	10	1.31	5	14	
150M-He	2000	86	1.6	–	1.27	5	14	H→He down to $30 M_{\odot}$ $M(\text{He})=29 M_{\odot}$
150M-bf	2000	86	9.1	10	1.31	5	9	Best-fitting
P150	1267	91	3.8	–	0.003	4	6	Original (Gilmer et al. 2017)
P150ni10	1267	91	9.3	10	1.37	10 ($X_{\text{Ni}}=0.14$)	9	
P150ni30	1267	91	9.3	10	1.37	30 ($X_{\text{Ni}}=0.045$)	9	
P150ni50	1267	91	9.3	10	1.4	50 ($X_{\text{Ni}}=0.015$)	9	
P150-bf	1267	91	9.3	10	1.37	1.6	9	Best-fitting
He90	18	90	–	–	1.3	25	29	Original (Heger & Woosley 2002)
He90-H001	18	90	1.6	10 ($X_{\text{H}}=0.01$)	1.3	25	29	
He90-H01	18	90	7.3	10 ($X_{\text{H}}=0.1$)	1.3	25	29	
He90-H02ni	18	90	9.7	10–60 ($X_{\text{H}}=0.2$) >60 ($X_{\text{H}}=0.05$)	1.4	2	29	Centred ^{56}Ni

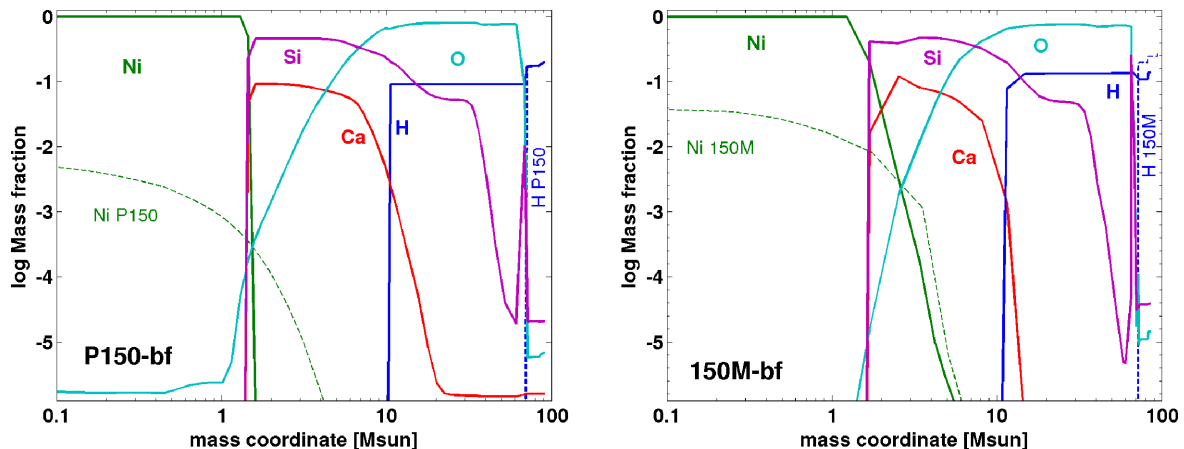


Figure 1. Distribution of selected species (hydrogen, oxygen, silicon, calcium and ^{56}Ni) in the modified models P150-bf (left) and 150M-bf (right). Dashed lines represent the distribution of hydrogen and ^{56}Ni in the original models P150 and 150M.

(Blinnikov et al. 2006; Kozyreva et al. 2014a). We mapped the models into STELLA when the shock is at the bottom (models 150M) or in the middle (models P150) of the H–He envelope. The energy of the pair-instability explosion (in the modified models) was increased by multiplying the velocity of the basic model (150M and P150) by a factor of 1.3. In the present simulations, we use 100 frequency bins. The opacity includes photoionization, free–free absorption, electron scattering processes assuming local thermodynamical equilibrium in the plasma, and line interactions. The line opacity is calculated using a data base of about 160 000 spectral lines from Kurucz & Bell (1995) and Verner, Verner & Ferland (1996). Energy deposition from ^{56}Ni and ^{56}Co radioactive decay is treated in a one-group diffusion approximation according to Swartz, Sutherland & Harkness (1995).

When calculating opacities, STELLA treats only a limited set of species, which generally play an important role in SNe. These are H, He, C, N, O, Ne, Na, Mg, Al, Si, S, Ar, Ca, stable Fe, which represent heavy iron-group elements, radioactive ^{56}Co and stable Ni and radioactive ^{56}Ni . We note that ejecta models extracted from STELLA, and used for the spectral synthesis post-processing

described in the following section, are limited to the same set of species.

2.3 Spectral synthesis

To obtain spectral time series for the models P150-bf and 150M-bf, we use the Monte Carlo radiative transfer code ARTIS (Kromer & Sim 2009). Using a detailed wavelength-dependent opacity treatment, ARTIS solves the time-dependent radiative transfer problem in homogeneously expanding SN ejecta. This includes a detailed simulation of the propagation of γ -ray photons and ultraviolet-optical-infrared photons. For γ -ray photons ARTIS accounts for interactions with matter by Compton scattering, photoelectric absorption and pair production (Sim & Mazzali 2008). For ultraviolet-optical-infrared photons ARTIS accounts for electron scattering, free–free, bound–free and line interactions. The latter are treated in the Sobolev approximation (Sobolev 1957) using a generalized scheme that enforces statistical equilibrium and allows for a parameter-free treatment of line fluorescence (Lucy 2002, 2003). The ionization and thermal

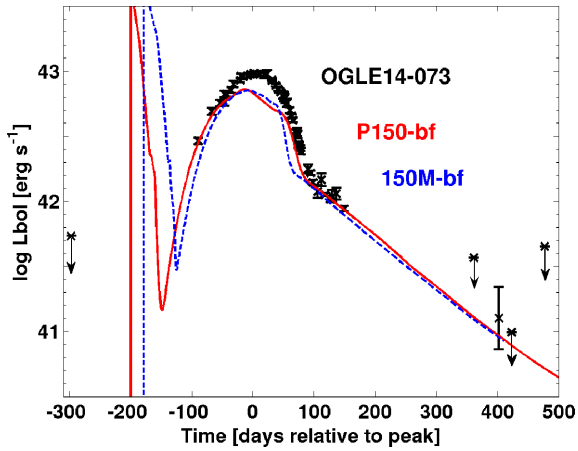


Figure 2. Bolometric light curve of OGLE14-073 (black crosses), compared to the synthetic STELLA light curves for models 150M-bf (blue dashed) and P150-bf (red solid).

balance equations are solved self-consistently with the radiative transfer problem. Excitation is treated approximately by assuming local thermodynamic equilibrium.

As input model for our ARTIS simulations we use the density and abundance structure from STELLA at 10 d after explosion, when the ejecta approach homologous expansion. In ARTIS this ejecta structure is mapped to a 100^3 uniform Cartesian grid and follows homologous expansion. On this grid, we then simulate the evolution of the radiation field by propagating 4×10^7 Monte Carlo quanta for 150 logarithmically spaced time-steps from 50 to 450 d past explosion. Once the Monte Carlo quanta escape from the simulation domain they are binned in time and on a logarithmic wavelength grid spanning 1 000 bins from 375 to 30 000 Å to obtain the spectral time series.

For our simulation we use an atomic data set that is based on the cd23_gf-5 model of Kromer & Sim (2009) but extended by H lines which were not part of the original compilation. The cd23_gf-5 data set is based on the atomic line list by Kurucz & Bell (1995). A grey approximation is used in optically thick cells for $t < 105$ d to speed up the calculations (cf. Kromer & Sim 2009). Local thermodynamic equilibrium is assumed for $t < 58$ d. At later epochs, we use the detailed ionization treatment of ARTIS to solve the ionization balance as described by Kromer & Sim (2009). For the excitation balance we follow a different approach and adopt a nebular approximation

$$\frac{n_{i,j,k}}{n_{0,j,k}} = W \frac{g_{i,j,k}}{g_{0,j,k}} \exp\left(-\frac{\epsilon_{i,j,k} - \epsilon_{0,j,k}}{k_B T_R}\right) \quad (1)$$

with symbols as defined in Kromer & Sim (2009). For metastable levels (i.e. levels without permitted electric dipole transitions to the ground state) the dilution factor W is set to 1.

3 RESULTS AND DISCUSSION

3.1 Bolometric properties and broad-band magnitudes

In Figs 2 and 3, we show our best-fitting synthetic light curves from the STELLA calculations for our modified models 150M-bf and P150-bf. Bolometric light curves and the evolution in the B , V , R and I bands are shown, respectively. The models qualitatively follow the observed light-curve evolution of OGLE14-073. In particular, the slope during the rise to the peak, the smooth dome-like shape of the peak phase, the drop after the peak and transition to the tail are well-

reproduced. The bolometric luminosity at peak is underestimated by 0.15 dex compared to OGLE14-073. The light curves are redder by 0.9 and 0.4 mag in B for 150M-bf and P150-bf, respectively. In V and R , both models are too red by 0.3 mag while a perfect match between models and observations is achieved in the I band. This colour effect could be related to the LTE assumption in STELLA or its simplified treatment of line opacities. For other PISN models it was suggested that the red colours result from line blanketing due to the high metal content of the models, particularly of ^{56}Ni (Dessart et al. 2013). As ^{56}Ni is confined to the central ejecta regions in our model, we expect the effect of line blanketing to be much weaker. In fact, our synthetic spectra presented in Section 3.2 are in good agreement with the broad-band SED observed in OGLE14-073.

In the following, we present our findings when exploring the various modifications of the original PISN models, in particular with respect to the bolometric light curve. Specifically, we investigate the consequences of changes of the amount of ^{56}Ni and hydrogen mixing, varying the explosion energy and the radius of the progenitor. The resulting trends are illustrated in Figs 4–6:

(i) Larger radius (model 150M-3000R) and higher energy (150M-14foe) for the model 150M increase the luminosity during the cooling phase after shock breakout and extend its duration as shown in Fig. 4. As there are no data between the non-detection limit (160 d before maximum) and the first discovery observation, the cooling phase cannot be well constrained.

(ii) A higher explosion energy reduces the diffusion time ($t_{\text{diff}} \sim 1/E$; Arnett 1982), hence, the light curve peaks earlier. We demonstrate this effect with the model 150M-14 foe which is the same as 150M-bf but with the explosion energy increased by 5 foe (see Fig. 4). 150M-14foe peaks 50 d earlier than our best-fitting model 150M-bf.

(iii) The deeper hydrogen is mixed into the ejecta, the broader is the dome-like maximum phase. Hydrogen remains the main element providing electrons and contributing to the total opacity via electron scattering. Therefore, substituting hydrogen with helium leads to a sharper rise to peak. We demonstrate the He-effect with model 150M-He (see Fig. 4).

(iv) Mixing of ^{56}Ni shortens the effective diffusion time and reduces the time between explosion and maximum light. We run model P150 with ^{56}Ni distributed uniformly in the innermost $10 M_{\odot}$ (model P150ni10), $30 M_{\odot}$ (model P150ni30) and $50 M_{\odot}$ (model P150ni50), and show the resulting light curves in Fig. 5. The resulting light curves have a shallower minimum after post-shock breakout cooling and in turn start rising earlier than the model P150-bf with centrally concentrated nickel. On top of that, the dome-like light curve loses the ‘OGLE14-073’ shape and tends to peak earlier, while the decline after the peak becomes flattened. We conclude that an extended distribution of ^{56}Ni makes the model less applicable to OGLE14-073.

To explore whether more compact models may improve the overall match between the synthetic and observed bolometric light curve, we carry out additional simulations based on the PISN model He90 from Heger & Woosley (2002). He90 is a compact ($18 R_{\odot}$) helium star model which produces $1.3 M_{\odot}$ of ^{56}Ni in the pair-instability explosion. Peak luminosity is reached 60 d earlier (about 100 d after the explosion) than for the hydrogen-rich models 150M-bf and P150-bf, as shown in Fig. 6. At the same time, the overall light curve becomes narrower and does not reproduce the slopes of the OGLE14-073 light curve. We test the model He90 with a modified chemical composition, i.e. with hydrogen mixed down to mass coordinate $M_r = 10 M_{\odot}$. The models He90-H001, He90-H01 and

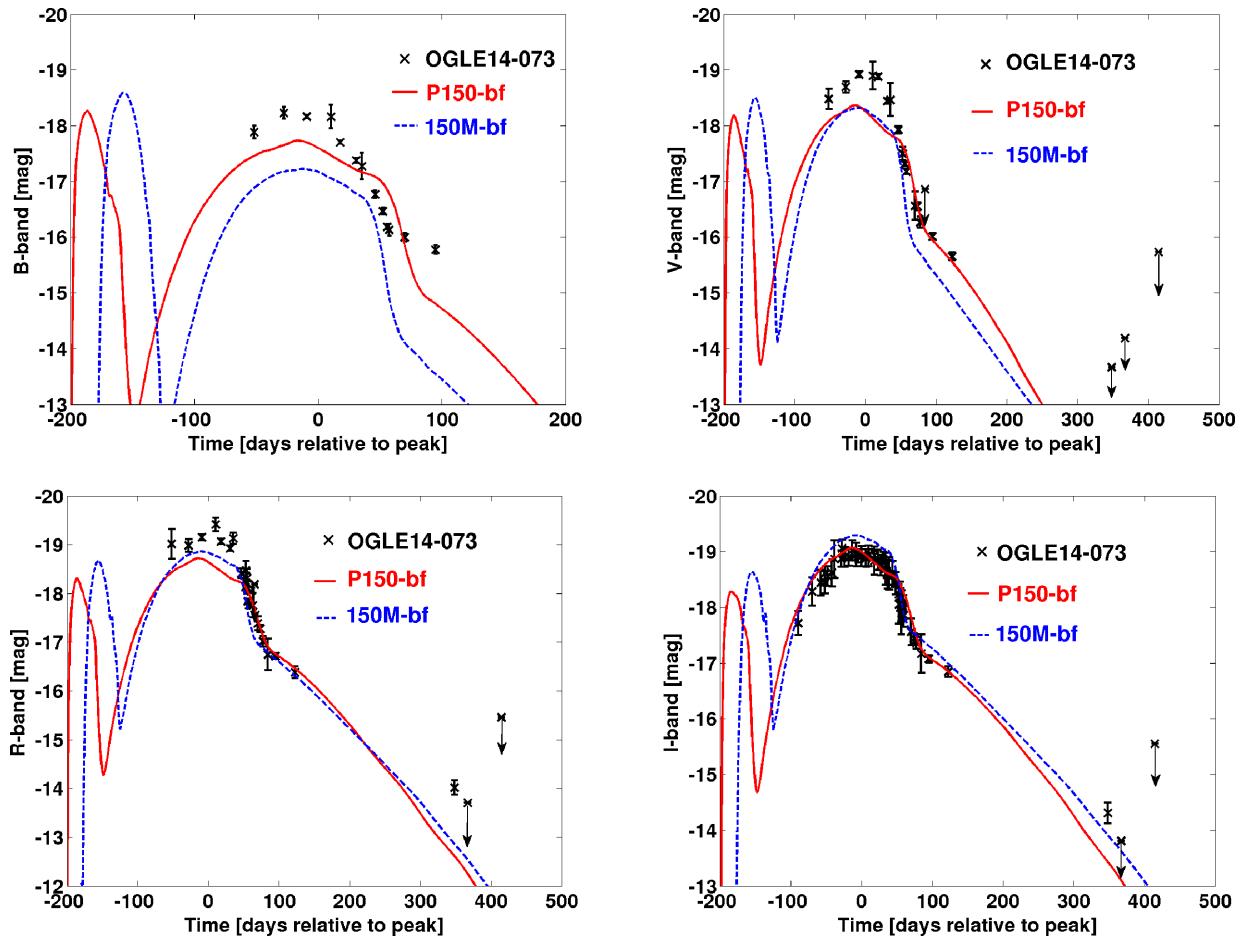


Figure 3. Light curves of OGLE14-073 (black crosses), compared to synthetic *STELLA* light curves for models 150M-bf (blue dashed) and P150-bf (red solid) in the *B* (upper left), *V* (upper right), *R* (lower left) and *I* (lower right) filter bands.

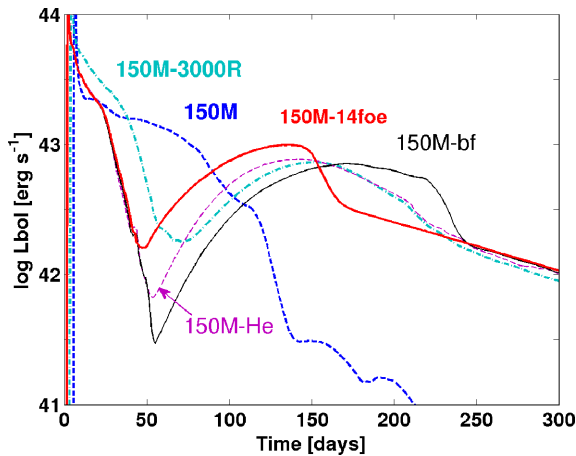


Figure 4. Bolometric light curves for the set of 150M models with different explosion energies, radii and hydrogen fraction.

He90-H02ni have different hydrogen mass fraction: 0.001, 0.1 and 0.2, correspondingly. We kept the original distribution of ^{56}Ni (it is naturally distributed in $20 M_{\odot}$) in the models He90, He90-H001 and He90-H01. In the model He90-H02ni, ^{56}Ni is located in the central $2 M_{\odot}$ to attempt to extend the rising phase of the light curve. Nevertheless, these modifications did not improve the match. We

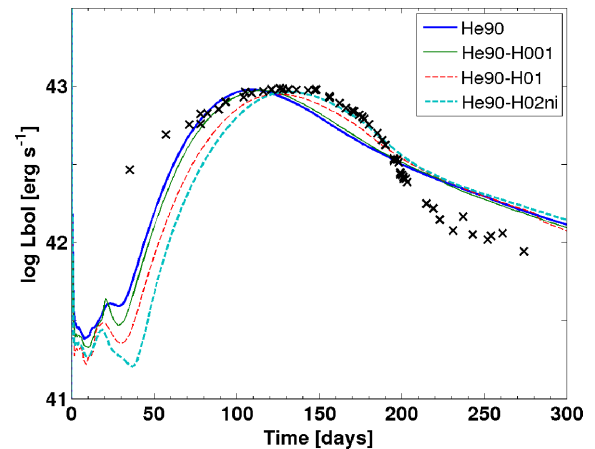


Figure 6. Bolometric light curves for the set of He90 models: He90 (solid thick, original), He90-H001 (solid thin, $X(\text{H}) = 0.01$), He90-H01 ($X(\text{H}) = 0.1$) and He90-H02ni ($X(\text{H}) = 0.2$, ^{56}Ni is confined to inner $2 M_{\odot}$). The data points of OGLE14-073 (black crosses) are shifted by 35 d (relative to the first detection). See details in Table 1.

conclude that the compact helium model He90 and its modifications do not result in observational properties that match OGLE14-073.

Before shifting our focus towards the spectral properties of OGLE14-073, we briefly summarize our findings based on mod-

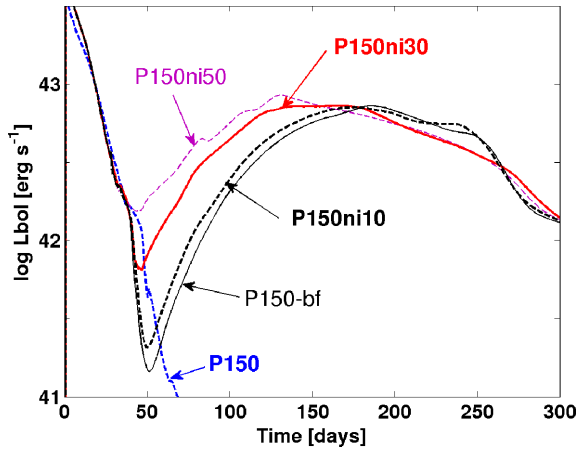


Figure 5. Bolometric light curves for the set of P150 models showing the influence of an extended ^{56}Ni distribution: the original model P150 (dashed), the best-fitting modified model P150-bf (thin), and the models P150ni10 (thick dashed), P150ni30 (thick), and P150ni50 (thin dashed) with ^{56}Ni distributed up to $M_r = 10, 30$ and $50 M_\odot$, correspondingly.

elling the bolometric and broad-band light curves. By modifying two first-principle PISN models, we are able to produce light curves that qualitatively reproduce the observed evolution of OGLE14-073. A crucial ingredient is to invoke down-mixing of hydrogen into the inner ejecta regions, similar to what has been observed for SN 1987A. As anticipated in the study of Terreran et al. (2017), a fairly high ^{56}Ni mass is needed to achieve a peak brightness similar to OGLE14-073. Unlike for SN 1987A, we do not require to mix radioactive ^{56}Ni from the centre to the outer ejecta regions. Instead, our best-fitting models have centrally located ^{56}Ni . Finally, the explosion energy and progenitor radius are somewhat unconstrained since they mainly affect the cooling phase, for which there is little observational information.

3.2 Spectral properties

For our best-fitting models P150-bf and 150M-bf we simulated the spectral evolution from 50 to 450 d with ARTIS and compared the synthetic spectra to those observed for OGLE14-073. A subset of these comparisons for both models is shown in Figs 7 and 8, respectively.

Fig. 7 shows synthetic spectra of model P150-bf for four epochs at day $-26, -7, 48$ and 115 relative to bolometric peak (the corresponding model epochs are 189, 208, 263 and 330 d past explosion, respectively). Overall, the agreement between P150-bf and OGLE14-073 is fairly good. The shape of the continuum in the model matches the observation between 4000 and 8000 \AA . However, there are minor (0.1 dex) differences in the flux level which correspond to an uncertainty in the distance estimate of about 15 per cent. The characteristic hydrogen lines are clearly visible in the synthetic spectra, and the shape of $H\alpha, H\beta$ and $H\gamma$ is in rough agreement with the shape of the observed line features in OGLE14-073. A closer inspection reveals that the detailed shape of the synthetic H lines is slightly too narrow compared to the observations. This may suggest insufficient ejecta velocities and in turn too low kinetic energies in the explosion. However, hydrogen at higher velocity, i.e. at a larger mass coordinate, leads to a different light-curve evolution inconsistent with the observed light curve of OGLE14-073. Uncertainties in the ionization/excitation structure may also affect the width of the hydrogen lines.

A clear difference between P150-bf and OGLE14-073 is visible to the blue of $H\alpha$. While the model spectrum shows an emission feature at around 6200 \AA that is originating from $\text{O I } \lambda 6159$, no such feature is present in OGLE14-073 at $-26, -7$ and 48 d. A similar behaviour is observed for $\text{O I } \lambda 5332$ that leads to a clear absorption feature in the model at around 5200 \AA but not in OGLE14-073. In contrast, both model and data show an absorption feature at around 5100 \AA . In the model this feature is due to Mg I and its strength increases with time, while in the data it is getting weaker.

Another difference between P150-bf and the observed spectra is visible in the Ca H&K absorption. Although present in OGLE14-073, the features are much weaker than those predicted from our model. This suggests too much Ca in the model. The major fraction of calcium is produced in the pair-instability explosion due to explosive oxygen and silicon burning, resulting in $0.4 M_\odot$ of Ca. However, there is also a small contribution resulting from progenitor metallicity. This leads to a Ca mass fraction at the 10^{-6} (1.5×10^{-6}) level up to the outermost ejecta layers (cf. Fig. 1), which owing to the intrinsic strength of the Ca H&K features gives rise to significant absorption. Also, there is a strong Ca infrared triplet feature in all synthetic spectra. In the corresponding spectral range, only in the last epoch data are available and again do not show such a strong feature.

Fig. 8 shows synthetic spectra of model 150M-bf for four epochs at day $-26, -7, 48$ and 115 relative to bolometric peak (the corresponding model epochs are 179, 198, 253 and 320 d past explosion, respectively). Similar to P150-bf, model 150M-bf also provides a reasonable match with OGLE14-073. The overall flux distribution in the observed range between 4000 and 8000 \AA agrees fairly well, and the H Balmer lines, which are the dominant line features in OGLE14-073, are clearly present in the model. As for P150-bf, the detailed line shapes of the Balmer lines of 150M-bf are also too narrow compared to OGLE14-073. In fact, 150M-bf has even narrower lines than P150-bf since the maximum ejecta velocity in 150M-bf is lower ($11\,000$ versus $16\,700 \text{ km s}^{-1}$). The strong emission feature at around 6200 \AA , which is not seen in OGLE14-073 and originates from $\text{O I } \lambda 6159$ in our models, is also present in 150M-bf.

Apart from these similarities between the two models, there are also important differences. While P150-bf shows a strong absorption in the Ca II H&K lines, this feature is absent in 150M-bf. This results from a different treatment of the progenitor metallicity in the initial models 150M and P150 (see Section 2.1), which leads to a different Ca distribution in the two models (see Fig. 1). In model 150M-bf, the Ca mass fraction drops to zero at a mass coordinate of $\sim 10.5 M_\odot$. In contrast, P150-bf contains Ca throughout the ejecta, though at a low-mass fraction of 1.5×10^{-6} in the outer layers. However, given the large ejecta mass and the high intrinsic strength of the Ca II H&K lines, this is sufficient to lead to strong Ca features in P150-bf.

Another difference between P150-bf and 150M-bf is the distribution of iron-group elements, specifically ^{56}Ni . In P150-bf the ^{56}Ni mass fraction drops abruptly at 1.6 solar masses, while 150M-bf shows a more gentle decline of ^{56}Ni (see Fig. 1). This leads to significant contributions from Fe lines (from the decay of ^{56}Ni) in the synthetic spectra of 150M-bf, while the optical spectra of P150-bf are still dominated by line features of intermediate-mass elements.

Despite some problems in the features associated with a few elements, we emphasize that the synthetic spectra of our best-fitting models provide overall a good match to the observations of OGLE14-073. In particular, we find good agreement in the continuum and thus also the broad-band colours. This is different from previously published PISN models (e.g. Dessart et al. 2013;

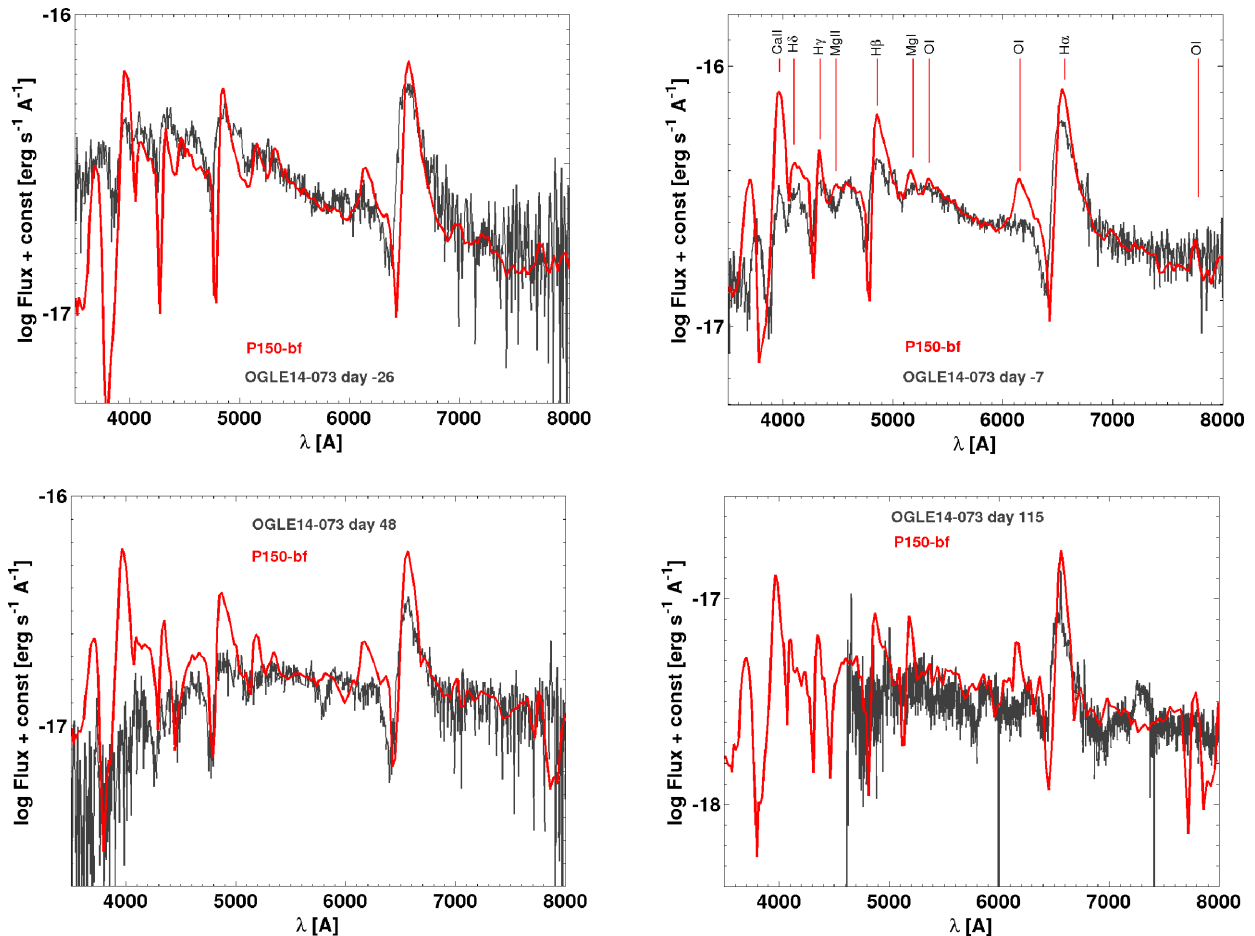


Figure 7. Synthetic spectra for model P150-bf (red) at day -26 , -7 , 48 and 115 relative to peak epoch. For comparison the observed spectra of OGLE14-073 at corresponding epochs are shown in black. The strongest features in the simulation are indicated in the day -7 spectrum.

Chatzopoulos et al. 2015; Jerkstrand, Smartt & Heger 2016), which, compared to observed SNe, suffered from a lack of flux at UV and blue wavelengths owing to strong line blanketing. Altogether, the good agreement found from our spectral and light-curve modelling make OGLE14-073 a very promising PISN candidate.

4 CONCLUSION

In this work, we have examined a possible PISN origin of the bright Type II SN OGLE14-073. As a starting point for our investigation, we use two first-principle PISN models with an initial progenitor mass $150 M_{\odot}$ at metallicity $Z = 0.001$. Modifications in the progenitor properties and ejecta structure enable a good match of the characteristic bolometric features of OGLE14-073. In particular, a relatively large mass of ^{56}Ni , in the range of $1.3\text{--}1.4 M_{\odot}$, was required to match the peak brightness. This increase is reasonable given the high sensitivity of the amount of ^{56}Ni synthesized during a PISN on small changes in the progenitor CO core mass as discussed in the Introduction. Furthermore, hydrogen must be mixed into the inner ejecta regions (down to a radial mass coordinate of $10 M_{\odot}$) to produce the characteristic dome-like shape of the OGLE14-073 light curve around peak. Such mixing is predicted by multidimensional explosion simulations and observed in SN 1987A, which shares some similarities with OGLE14-073. The best-fitting models thus constructed produce synthetic light curves which match the observed bolometric evolution of OGLE14-073 fairly well. In

particular, the dome-like structure around peaks is reproduced, as is the sharp post-peak drop-off and the settling on to the light-curve tail which seems to follow the characteristic radioactivity decline.

In addition to the good agreement in the bolometric light curve, our models P150-bf and 150M-bf also reproduce the observed spectral evolution of OGLE14-073 remarkably well. In particular, we find a good match to the overall SED and the broad-band colours from epochs well before peak to several weeks thereafter. This is different from previous PISN models, which suffer from a flux deficit in the blue wavelength regime owing to strong line blanketing by large amounts of iron-group elements in the ejecta. This effect is much less prominent in our models, since ^{56}Ni , the dominant iron-group species, is confined to the central region of the ejecta. Our synthetic spectra also reproduce many of the observed absorption features of OGLE14-073, specifically the prominent hydrogen Balmer lines. In detail, however, there are some differences in the line shapes. Given that the models have not been tuned to fit the spectra this is to be expected. Also, a more sophisticated radiative transfer treatment may lead to better agreement in the absorption features.

In summary, our best-fitting models produce synthetic observables that fit many characteristic features observed in OGLE14-073. In fact, the match between predicted and observed signatures reported here is significantly better than for previous PISN candidates (Dessart et al. 2013; Jerkstrand et al. 2017; Kozyreva et al. 2017). Consequently, we conclude not only that a PISN origin of

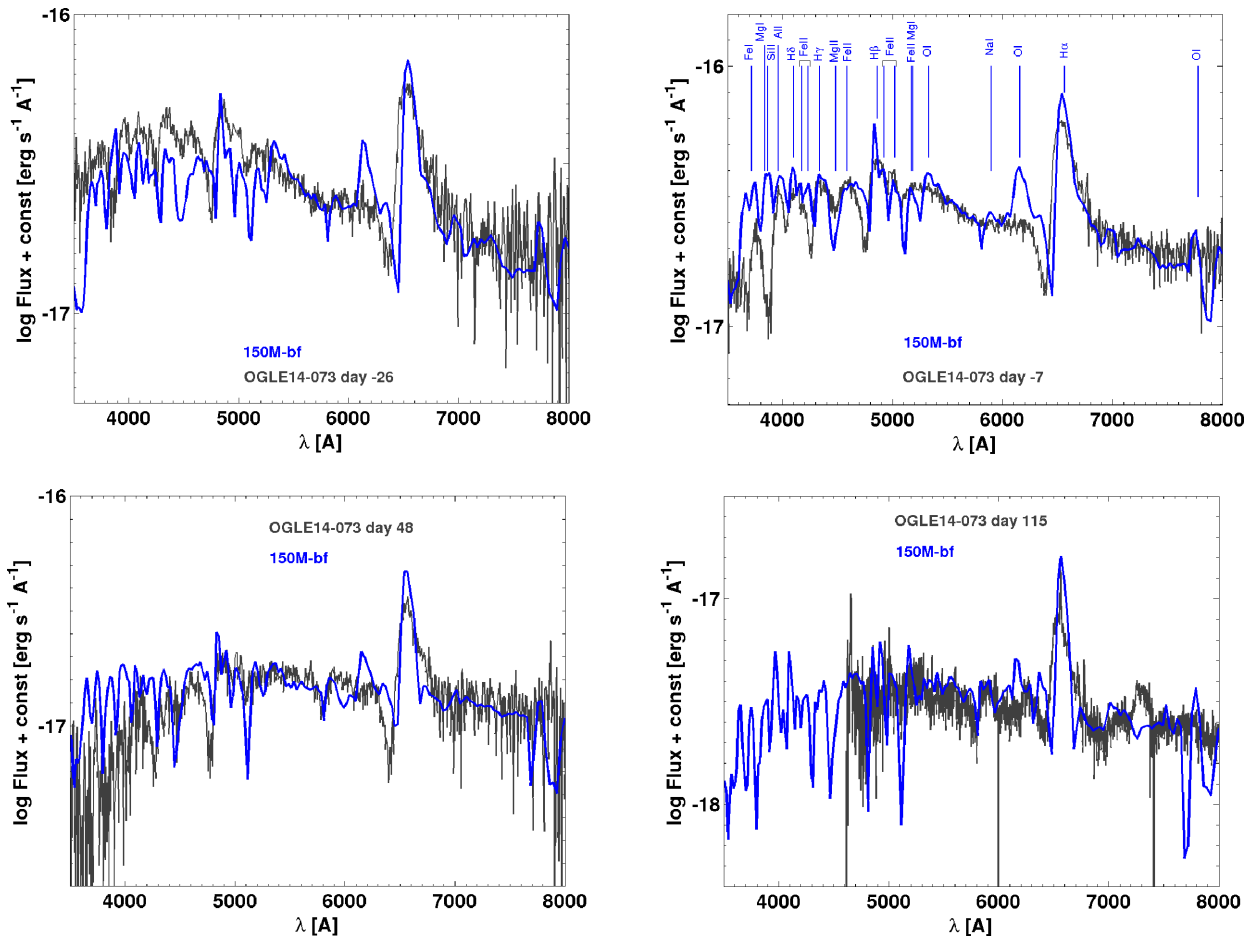


Figure 8. Same as Fig. 7 but for model 150M-bf, which is shown in blue.

OGLE14-073 is possible but that this bright SN is one of the most promising PISN candidates. Late-time nebular spectra may substantiate this interpretation. However, no such data are available for OGLE14-073, which faded fairly quickly after the last observations reported by Terreran et al. (2017).

ACKNOWLEDGEMENTS

The STELLA simulations were carried out on the DIRAC Complexity system (grants ST/K000373/1 and ST/M006948/1), operated by the University of Leicester IT Services, which forms part of the STFC DiRAC HPC Service (www.dirac.ac.uk). For the ARTIS simulations, we gratefully acknowledge the Gauss Centre for Supercomputing (GCS) for providing computing time through the John von Neumann Institute for Computing (NIC) on the GCS share of the supercomputer JUQUEEN (Stephan & Docter 2015) at Jülich Supercomputing Centre (JSC). GCS is the alliance of the three national supercomputing centres HLRS (Universität Stuttgart), JSC (Forschungszentrum Jülich), and LRZ (Bayerische Akademie der Wissenschaften), funded by the German Federal Ministry of Education and Research (BMBF) and the German State Ministries for Research of Baden-Württemberg (MWK), Bayern (StMWFK) and Nordrhein-Westfalen (MIWF). MK acknowledges support from the Klaus Tschira Foundation. UMN is supported by the Transregional Collaborative Research Centre TRR 33 ‘The Dark Universe’ of the German Research Foundation (Deutsche Forschungsgemeinschaft). RH acknowledges support from EU-FP7-ERC-2012-St

Grant 306901, the World Premier International Research Centre Initiative (WPI Initiative), MEXT, Japan, and the ‘ChETEC’ COST Action (CA16117). The authors thank Ryan Wollaeger (LANL, USA) for additional simulations with the spectral synthesis code SUPERNU.

REFERENCES

- Arnett W. D., 1982, *ApJ*, 253, 785
 Barkat Z., Rakavy G., Sack N., 1967, *Phys. Rev. Lett.*, 18, 379
 Blagorodnova N. et al., 2014, *Astron. Telegram* 6489
 Blinnikov S. I., Röpké F. K., Sorokina E. I., Gieseler M., Reinecke M., Travaglio C., Hillebrandt W., Stritzinger M., 2006, *A&A*, 453, 229
 Chatzopoulos E., Wheeler J. C., Couch S. M., 2013, *ApJ*, 776, 129
 Chatzopoulos E., van Rossum D. R., Craig W. J., Whalen D. J., Smidt J., Wiggins B., 2015, *ApJ*, 799, 18
 Dessart L., Audit E., 2018, *A&A*, 613, A5
 Dessart L., Waldman R., Livne E., Hillier D. J., Blondin S., 2013, *MNRAS*, 428, 3227
 Dubey A., Reid L. B., Weide K., Antypas K., Ganapathy M. K., Riley K., Sheeler D., Siegal A., 2009, preprint, ([arXiv:0903.4875](https://arxiv.org/abs/0903.4875))
 Ekström S. et al., 2012, *A&A*, 537, A146
 Fryxell B. et al., 2000, *ApJS*, 131, 273
 Gilmer M. S., Kozyreva A., Hirschi R., Fröhlich C., Yusof N., 2017, *ApJ*, 846, 100
 Heger A., Woosley S. E., 2002, *ApJ*, 567, 532
 Jerkstrand A., Smartt S. J., Heger A., 2016, *MNRAS*, 455, 3207
 Jerkstrand A. et al., 2017, *ApJ*, 835, 13

- Kozyreva A., Blinnikov S., Langer N., Yoon S.-C., 2014a, *A&A*, 565, A70
- Kozyreva A., Yoon S.-C., Langer N., 2014b, *A&A*, 566, A146
- Kozyreva A., Hirschi R., Blinnikov S., den Hartogh J., 2016, *MNRAS*, 459, L21
- Kozyreva A. et al., 2017, *MNRAS*, 464, 2854
- Kromer M., Sim S. A., 2009, *MNRAS*, 398, 1809
- Kurucz R., Bell B., 1995, Atomic Line Data, Kurucz CD-ROM No. 23., Smithsonian Astrophysical Observatory, Cambridge, Mass. <http://kurucz.harvard.edu/cdroms.html>
- Langer N., Norman C. A., de Koter A., Vink J. S., Cantiello M., Yoon S.-C., 2007, *A&A*, 475, L19
- Lodders K., 2003, *ApJ*, 591, 1220
- Lucy L. B., 2002, *A&A*, 384, 725
- Lucy L. B., 2003, *A&A*, 403, 261
- Moriya T. J., Terreran G., Blinnikov S. I., 2018, *MNRAS*, 475, L11
- Nomoto K., Shigeyama T., Kumaga S., Hashimoto M.-A., 1988, *Proc. Astron. Soc. Aust.*, 7, 490
- Rakavy G., Shaviv G., 1967, *ApJ*, 148, 803
- Sim S. A., Mazzali P. A., 2008, *MNRAS*, 385, 1681
- Sobolev V. V., 1957, *Svt. Astron.*, 1, 678
- Stephan M., Docter J., 2015, *J. Large-scale Res. Facilities*, 1, A1
- Swartz D. A., Sutherland P. G., Harkness R. P., 1995, *ApJ*, 446, 766
- Terreran G. et al., 2017, *Nat. Astron.*, 1, 713
- Utrobin V., 1993, *A&A*, 270, 249
- Verner D. A., Verner E. M., Ferland G. J., 1996, *Atomic Data Nuclear Data Tables*, 64, 1
- Vink J. S., 2015, Very Massive Stars in the Local Universe, Vol. 412, Astrophysics and Space Science Library, Springer International Publishing, Switzerland, p. 77
- Wongwathanarat A., Müller E., Janka H.-T., 2015, *A&A*, 577, A48
- Wyrzykowski L., Udalski A., Kozłowski S., Kostrzewa-Rutkowska Z., Szymanski M. K., Mroz P., Soszynski I., 2014, *Astron. Telegram*, 6494
- Yusof N. et al., 2013, *MNRAS*, 433, 1114

This paper has been typeset from a $\text{T}_{\text{E}}\text{X}/\text{L}^{\text{A}}\text{T}_{\text{E}}\text{X}$ file prepared by the author.